Vertical asymmetry and the ripple-rotation transition in epitaxial growth and erosion on (110) crystal surfaces

Artem Levandovsky* and Leonardo Golubović
Physics Department, West Virginia University, Morgantown, West Virginia 26506-6315, USA
(Received 8 May 2007; published 19 October 2007)

Vertical (up-down) asymmetry is ubiquitous feature of the nonequilibrium statistical mechanics of realistic growing interfaces. Yet, the actual role of vertical asymmetry (VA) in epitaxial growth on crystal surfaces is still elusive. Is vertical asymmetry a primary or secondary factor in epitaxial growth and erosion? Can vertical asymmetry alone produce major qualitative effects on long length scale interface morphologies? To address these questions in depth, we theoretically discuss the effects of vertical growth asymmetry on far-from-equilibrium interfacial morphologies occurring in the epitaxial growth and erosion of (110) crystal surfaces. We theoretically elucidate the so-called ripple rotation transition on the Ag(110) crystal surface [F. B. de Mongeot *et al.*; Phys. Rev. Lett. **84**, 2445 (2000), G. Constantini *et al.*, J. Phys.: Condens. Matter **13**, 5875 (2001)], as the transition between the rectangular rippled states (checker-board structures of alternating rectangular pyramids and pits). We show that the experimental surface diffraction data seen in this transition can be understood only by invoking vertical growth asymmetry. In the proximity of the transition point, we find that vertical asymmetry itself produces an interface morphology yielding a four-lobe near in-phase diffraction pattern having four peaks along the principal axes of the (110) surface, in accord with the experiments on Ag(110). Moreover, on the two sides of the ripple rotation transition, we find two exotic interface states induced by vertical asymmetry, which correspond well /to the interface morphologies seen on Ag(110). We document our results by numerical simulations and by analytic arguments. Our theoretical findings, in combination with experiments, provide the first rigorous evidence that VA plays a significant role in epitaxial growth and erosion on crystal surfaces.

DOI: 10.1103/PhysRevE.76.041605 PACS number(s): 81.10.−h

I. INTRODUCTION

Properties and dynamics of thin films surfaces are naturally affected by the difference between the media and processes going on above and below film interface. This up-down vertical asymmetry (VA) has to be incorporated into any realistic model of interface dynamics. Epitaxial growth and erosion phenomena [1–10], such as those studied in this paper, are not exceptions to this. VA effects are clearly visible on the interfaces of homoepitaxially grown films, for example, through the difference between the shapes of pyramids and pits (upside-down pyramids) that develop during the homoepitaxial growth on (100) and (111) crystal surfaces [11]. The primary cause for the formation of these fascinating structures is the classical Ehrlich-Schwoebel-Villain (ESV) instability [7]. To this date, however, the actual potential of VA to affect the interface morphology and dynamics of epitaxial growth and erosion remains unexplored. Experimentally, due to ubiquitous presence of VA, it is impossible to "switch VA off" in order to see how much this effect really matters. Interestingly, major effects here, such as the ESV effect and slope stabilizing effects, themselves do not introduce VA in a fundamental way (see Sec. II). Moreover, under some circumstances, continuum modeling of epitaxial growth and erosion reproduces major features of the experimentally observed interface dynamics (e.g., coarsening exponents) even with VA effects ignored [6]. One is then naturally lead to ask a basic question. Is VA primary or a secondary factor in epitaxial growth and erosion? Notably, it is hard to address this question by using microscopic (quasiatomistic) modeling of the epitaxial growth phenomena, such as kinetic Monte Carlo simulations or other similar approaches [10]. Very similar to the experiments, realistic microscopic simulations of epitaxial growth ubiquitously include VA and thus can not be used to directly extract VA effects *per se* (separately from other effects). This is explicitly evidenced by the step flow modeling of epitaxial growth recently discussed by Li and Evans [5]. In addition to the ESV and slope selection terms of the surface current, they obtain also VA current term which is generally nonzero [5]. Thus, within microscopic modeling, one cannot eliminate (switch off) VA effects while still remaining within a physically acceptable model for epitaxial growth.

In this study, we pursue a conceptually different approach based on the phenomenological continuum modeling of interface dynamics [4–6,8,9]. Within this approach, the interface is described by its heights evolution equation, generally of the form

$$\frac{\partial h(\vec{x},t)}{\partial t} = v(h) \tag{1.1}$$

with $v(h)$ being the local inteface height velocity (as in prevous studies [4–9], here we employ the frame comoving with the interface). $v(h)$ is a functional of the interface heights $h(\vec{x},t)$. In the absence of VA, the interface velocity $v(h)$ is an odd functional of the interface heights $v(-h) = -v(h)$ and, therefore, vertical reflection $h \to -h$ becomes a

*Present address: Department of Chemical and Petroleum Engineering, University of Pittsburgh, Pittsburgh, PA 15261.

dynamical symmetry of the interface evolution equation (1.1). With such a model, for example, there would be no shape differences between pyramids and pyramdal pits (upside-down pyramids). However, in reality, VA is ubiquitously present. Thus, for realistic interface dynamics models $v(-h) \neq -v(h)$, and the interface velocity can be generally decomposed as

$$v(h) = v_{\mathrm{VS}}(h) + v_{\mathrm{VA}}(h). \tag{1.2}$$

Here, $v_{\mathrm{VS}}(h) = -v_{\mathrm{VS}}(-h) = [v(h) - v(-h)]/2$ and $v_{\mathrm{VA}}(h) = v_{\mathrm{VA}}(-h) = [v(h) + v(-h)]/2$ are, respectively, odd and even parts of $v(h)$. The *even* part, $v_{\mathrm{VA}}(h)$ breaks the vertical reflection ($h \rightarrow -h$) symmetry of the interface dynamics and thus introduces the VA effects which are of primary interest in the present study. The separation between different symmetry contributions in the continuum model Eq. (1.2) directly allows to extract generic VA effects simply by comparing the results obtained with nonzero VA to those obtained with zero VA. Such a comparison is virtually impossible both in experiments and in microscopic kinetic simulations.

Here, we will explore still largely elusive VA role in epitaxial growth by considering in depth VA effects on the growth and erosion on (110) crystal surfaces. Recent experimental studies have revealed a number of intriguing far-from-equilibrium interfacial structures developing on these surfaces, both in growth [1] and in ion beam erosion experiments [2,3]. Understanding these structures is a challenging yet experimentally very interesting problem of the nonequilibrium statistical mechanics. It has been addressed theoretically within a continuum phenomenological theory, however, with no VA effects incorporated [4]. Even so, this theory has provided new and interesting insights such as the prediction of the so-called rhomboidal pyramid interface state which has been indeed seen in the subsequent experiments on (110) surfaces of copper and rhodium [3]. Unlike the epitaxial growth phenomena on high symmetry (100) and (111) surfaces on which growing pyramidal structures form [5,6,8,9], on low symmetry rectangular (110) surfaces, the dominant interfacial structures formed due to the ESV instability are the rippled states [1–3]. They are wavelike, seemingly one-dimensional periodic structures, seen in the experiments of de Mongeot and co-workers, on (110) crystal surfaces of silver, copper, and rhodium [1–3]. Rippled state wave-vector points along one of the two principal (high symmetry) directions of the (110) surface. Experimentally, rippled state interface Fourier transform (FT) magnitude (obtained from near in-phase surface diffraction patterns) has a single pair of peaks which are at two opposite q vectors along the principal directions of (110) [1]. In addition, the interface slope distribution (SD) (obtained from out-of-phase diffraction patterns), for a rippled state also exhibits a pair of peaks (doublet) that are along one of the two high symmetry surface directions. This suggests that rippled state interface has a zig-zag profile comprised of facets with alternating (in sign) slopes. The slope vectors of these facets are along one of the two principal directions of the (110) crystal surface. Thus, depending on the choice of the preferred facet direction, there are two major kinds of the rippled states R_1 and R_2 [4]. In contrast to the high symmetry (100) surfaces, the two principal directions of (110) surfaces are not equivalent (symmetry related). Due to this, most commonly, only one of the two rippled states, R_1 or R_2 occurs under given experimental conditions. By changing these conditions, such as substrate temperature, deposition (or erosion) flux intensity and molecular beam energy, de Mongeot and co-workers were able to drive far-from-equilibrium transitions between the two kinds of rippled states [1–3]. Both the experiments [1–3] and the theory [4] have evidenced a complex character of this so-called ripple rotation (by 90°) transition. In general, the transition goes through the formation of intermediary states, such as the aforementioned rhomboidal pyramid (RhP) state.

The present study is devoted to the statistical mechanics of an alternative scenario of the ripple rotation transition which is realized in the experiments on the Ag(110) surface, both in the epitaxial growth [1] and in the erosion studies [2]. In these systems, the ripple rotation transition occurs in a multistable system parameter range, in which both types of the rippled state facets, R_1 and R_2 are locally stable. Due to this multistability, the simple rippled states R_1 and R_2 are replaced by more complex structures, the so-called rectangular rippled states $R_1^{(\mathrm{rec})}$ and $R_2^{(\mathrm{rec})}$ [4]. These interface states are checker-board structures of alternating rectangular pyramids and pits, see Fig. 1. Unlike, for example, the simple R_1 rippled state, a rectangular pyramid of the $R_1^{(\mathrm{rec})}$ state incorporates not only the long R_1 facets but also significantly smaller metastable R_2 facets [4]. Our rippled rectangular pyramid structures in the Fig. 1 can indeed be seen in the STM images obtained in the erosion experiments on Ag(110) [see Fig. 4(d) of Ref. [2]].

We will show here that the experimental surface diffraction patterns and underlying surface morphologies seen in this far-from-equilibrium transition on Ag(100), are qualitatively strongly affected by vertical growth asymmetry; see Secs. II and III. Theoretical findings of the present paper, in combination with the experimental data in Refs. [1,2], provide the first clear cut evidence that VA plays a significant role in epitaxial growth and erosion on crystal surfaces. While it has been long known that, for example, on the (100) surfaces, VA produces experimentally seen differences between the shapes of four sided pyramids and pits (inverted pyramids) [11], actual VA effects on interface structure and dynamics are still inconclusively debated and remain elusive. In fact, some real (and likely still incomplete) understanding of VA structural and dynamical effects has begun to emerge only recently, for the case of high symmetry (100) surfaces [6]. Here, we discuss, in depth, VA effects on low symmetry (110) crystal surfaces. We find that VA plays an essential role in the multistable range in which the rippled rectangular states form. Interestingly, we find that, due to VA, the ripple rotation transition is smeared and occurs over an extended parameter range: The transition point at which the qualitative change of near in-phase diffraction patterns occurs turns out to be different from the transition point at which the qualitative change of out-of phase diffraction patterns occurs. At the former transition point, we find the four-lobe near in-phase diffraction pattern with the four peaks along the principal axes of the (110) surface, in accord with the experiments on

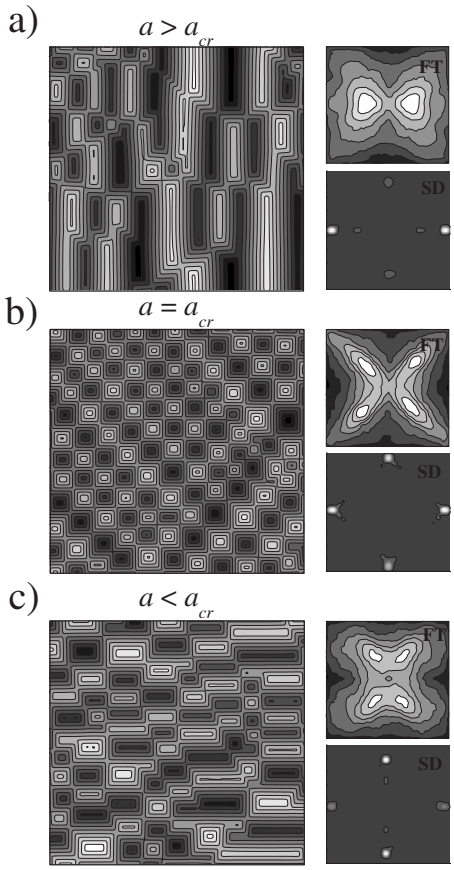

FIG. 1. Ripple rotation transition between the rectangular rippled states $R_1^{(\mathrm{rec})}$ and $R_2^{(\mathrm{rec})}$, for zero VA. The figure gives interface morphologies (through surface contour plots) and the standard surface diffraction data: interface slope distributions (SD) and Fourier transform (FT) magnitudes. The two $R^{(\mathrm{rec})}$ states are checkerboard structures of alternating rectangular rooftoplike pyramids and pits (inverted rooftops). For $a<a_{\mathrm{cr}}$, the $R_2^{(\mathrm{rec})}$ state develops, in a), whereas for $a>a_{\mathrm{cr}}$ the $R_1^{(\mathrm{rec})}$ state develops, in c). Here, a is a temperaturelike control parameter, see the text. At the very transition point ($a=a_{\mathrm{cr}}$), for zero VA, the interface is a checkerboard structure of alternating four-sided pyramids and pyramidal pits, yielding the FT with four peaks at $(\pm q_1, \pm q_2)$, see b).

Ag(110) [1], see Sec. III. Such a pattern and the underlying surface morphology are different from those occurring with zero VA [seen in Fig. 1(b)]. This theoretical finding, and its consistency with the experiments, show that VA itself can induce formation of unique surfaces morphologies that would be absent with zero VA. Moreover, on the two sides of the extended ripple rotation transition, we find two interesting interface states which are qualitatively altered forms of the rectangular rippled states (see Secs. II and III). These two interface states are both induced by the VA presence, and correspond well to the interface morphologies seen in the STM images of Ref. [2]. One of them exhibits an enhanced roughening which was indeed seen in the experiments on Ag(110) surface [2]. This intensely rough interface state is an exotic alteration of the rectangular rippled $R_1^{(\mathrm{rec})}$ state, with rectangular pyramids replaced by arrays of small (nearly) square shaped pyramids packed between long rectangular pits. The other interface state revealed here is an altered form of the rectangular rippled $R_2^{(\mathrm{rec})}$ state. It has depressed pit sizes, whereas the rooftop edges of elongated wormlike mounds are decorated by fascinating arrays of small rounded mounds. Unlike the former, this latter state does not exhibit enhanced roughening. Due to this difference between the roughening characters of the two exotic states, the interface data are highly asymmetric across the ripple rotation transition, as was indeed seen in the experiments on Ag(110) [1,2]. We document our results by numerical simulations and by analytic arguments applied to a general continuum model for the growth and erosion of (110) crystal surfaces.

The layout of this paper is as follows. In Sec. II, we conceptually and analytically discuss the effects of VA on the interface dynamics in epitaxial growth. At the end of Sec. II and in Sec. III, we corroborate our analytic discussions by numerical simulations. In Sec. IV we summarize our theoretical results and compare them with the growth and erosion experiments on the Ag(110).

II. INTERFACE DYNAMICS AND VERTICAL ASYMMETRY

Under conditions typical for epitaxial growth, the interface heights $h(\vec{x},t)$, above the film base [with $\vec{x}=(x_1,x_2)$, the film base vector], obey a conservation law. In the absence of desorbtion, vacancies, or overhangs, all relaxation processes on the surface conserve the deposited volume of the growing film. Thus, in the frame comoving with the interface, the height evolution equation (1.1) is of the form

$$\frac{\partial h(\vec{x},t)}{\partial t} = v(h) = -\vec{\nabla}\cdot\vec{J} = -\frac{\partial J_1}{\partial x_1} - \frac{\partial J_2}{\partial x_2}, \tag{2.1}$$

where $\vec{J}$ is the surface current [5–9]. It can be written as

$$\vec{J} = \vec{J}^{\mathrm{NE}}(\vec{\nabla}h) + \vec{J}^{(\mathrm{curv})}. \tag{2.2}$$

Here, $\vec{J}^{\mathrm{NE}}(\vec{\nabla}h)$ is the nonequilibrium surface current which is a function of the local interface slope vector $\vec{M}=\vec{\nabla}h=(M_1,M_2)$, with $M_1=\partial h/\partial x_1$ and $M_2=\partial h/\partial x_2$ [4–6,8,9]. In contrast to $\vec{J}^{\mathrm{NE}}$ current, $\vec{J}^{(\mathrm{curv})}$ in Eq. (2.2) is a "curvature current" which vanishes on flat interfaces ("facets") for whatever slope $\vec{M}=\vec{\nabla}h$ they have. It has the form

$$\vec{J}^{(\mathrm{curv})} = \vec{J}_{\mathrm{SD}} + \vec{J}_{\mathrm{VA}}. \tag{2.3}$$

Here, $\vec{J}_{\mathrm{SD}} \sim \vec{\nabla}(\nabla^2 h)$ is a contribution isomorphic to the Mullins' surface diffusion current, whereas the second term in Eq. (2.3) is the vertical asymmetry current. It has been suggested originally by Villain [7], in the form

$$\vec{J}_{\mathrm{VA}} \sim \vec{\nabla}(\vec{\nabla}h)^2,$$

which is even under $h\rightarrow -h$ and thus produces an even contribution to the interface velocity introducing VA into interface dynamics; see Eq. (1.2). In contrast to $\vec{J}_{\mathrm{VA}}$, both the nonequilibrium and Mullins' surface diffusion currents are

both odd under the vertical reflection $h \to -h$ and thus do not contribute any VA. In particular, the nonequilibrium current $\vec{J}^{\mathrm{NE}}(\vec{\nabla} h)$ (which encodes the significant ESV instability and other effects stabilizing the preferred slopes [4–6,8,9]) does not break the vertical symmetry for the following fundamental reason: By assuming normal flux incidence, one must have $\vec{J}^{\mathrm{NE}}(-\vec{M}) = -\vec{J}^{\mathrm{NE}}(\vec{M})$ due to the symmetry of major crystal surfaces [such as (100), (111), and (110)] under the "horizontal"(base plane) inversion $\vec{x} \to -\vec{x}$. It is then not hard to see that, as $\vec{M} = \vec{\nabla} h = \partial h / \partial \vec{x}$, the horizontal inversion symmetry incidentally implies that $\vec{J}^{\mathrm{NE}}$ must change sign also under the "vertical" reflection $h \to -h$ (with $\vec{x}$ unchanged). Thus, incidentally, the nonequilibrium current $\vec{J}^{\mathrm{NE}}(\vec{\nabla} h)$ does not introduce any VA. In view of this, the fundamental growth features, such as the allowed values of preferred facet slopes vectors [encoded in the form of $\vec{J}^{\mathrm{NE}}(\vec{\nabla} h)$ through its stable zeros [4–9]] are insensitive to VA. One thus arrives at a striking conclusion that the major growth factors, such as the Ehrlich-Schwoebel-Villain instability and slope stabilizing effects modeled by $\vec{J}^{\mathrm{NE}}(\vec{\nabla} h)$, themselves do not introduce VA in a fundamental way. Nonetheless, the VA is ubiquitously present in realistic systems: the putative up-down reflection $h \to -h$ is not a symmetry of any realistic interface dynamics. Due to VA, the shapes of pyramids and pits are not simply related to each other by the upside-down reflection. Yet, potential effects of VA are still uncertain and poorly understood. Can VA alone produce major qualitative effects on long length scale interface morphologies? As noted above, the possible values of preferred facet slopes vectors [corresponding to the set of stable zeros of $\vec{J}^{\mathrm{NE}}(\vec{\nabla} h)$ [4–9]] are insensitive to VA. However, which ones of these many zeros are going to be selected during interface growth is generally not encoded in the form of $\vec{J}^{\mathrm{NE}}(\vec{\nabla} h)$ [such as the one in Eq. (2.6) in the following]. Unless some special restrictions, not generic to epitaxial growth process, are arbitrarily imposed on the form of the surface current (e.g., the existence of an effective free energy generating the model dynamics), the very selection of preferred facets out of the set of all allowed facets [corresponding to all stable zeros of $\vec{J}^{\mathrm{NE}}(\vec{\nabla} h)$] will be kinetically decided during the surface evolution. Due to this feature, the kinetic VA effects may potentially play qualitatively important role in determining the form of large scale structures of the growing interfaces in epitaxial growth and erosion.

To proceed, we note that above-mentioned Villains's VA current contributes the so-called conservative Kardar-Parisi-Zhang (CKPZ) term $-\vec{\nabla} \cdot \vec{J}_{\mathrm{VA}} \sim -\nabla^2 (\vec{\nabla} h)^2$ to the interface velocity in Eq. (2.1). Here, this term is exhibited in the form applicable to isotropic surfaces. For the rectangular symmetry (110) surfaces, the forms of $\vec{J}_{\mathrm{VA}}$ and of the corresponding conservative CKPZ term are more complex. By respecting the symmetries of (110) surfaces, we find that VA contributes to the interface velocity Eq. (2.1) the CKPZ term of the general form

$$-\vec{\nabla} \cdot \vec{J}_{\mathrm{VA}} = -\frac{\lambda_{11}}{2}\left(\frac{\partial}{\partial x_1}\right)^2 \left(\frac{\partial h}{\partial x_1}\right)^2 - \frac{\lambda_{12}}{2}\left(\frac{\partial}{\partial x_1}\right)^2 \left(\frac{\partial h}{\partial x_2}\right)^2 - \frac{\lambda_{21}}{2}\left(\frac{\partial}{\partial x_2}\right)^2 \left(\frac{\partial h}{\partial x_1}\right)^2 - \frac{\lambda_{22}}{2}\left(\frac{\partial}{\partial x_2}\right)^2 \left(\frac{\partial h}{\partial x_2}\right)^2 - \frac{\lambda_3}{2}\frac{\partial}{\partial x_1}\frac{\partial}{\partial x_2}\left[\frac{\partial h}{\partial x_1}\frac{\partial h}{\partial x_2}\right], \tag{2.4}$$

which is, again, even in h, in contrast to the surface diffusionlike (Mullins) current $\vec{J}_{\mathrm{SD}}$, which on (110) surfaces contributes to the interface velocity (2.1) the term of the general form

$$-\vec{\nabla} \cdot \vec{J}_{\mathrm{SD}} = -\kappa_{11}\left(\frac{\partial}{\partial x_1}\right)^4 h - 2\kappa_{12}\left(\frac{\partial}{\partial x_1}\right)^2 \left(\frac{\partial}{\partial x_2}\right)^2 h - \kappa_{22}\left(\frac{\partial}{\partial x_2}\right)^4 h, \tag{2.5}$$

which is odd in h. In Eq. (2.5), for the (110) crystal surface, the constants $\kappa_{\alpha\beta}$ are generally unequal to each other [4]. The VA contribution to the interface velocity exhibited in Eq. (2.4) is consistent with the symmetries of the (110) surface. They require Eq. (2.4) to be invariant under the two reflections: (i) $(x_1, x_2) \to (-x_1, x_2)$ and (ii) $(x_1, x_2) \to (x_1, -x_2)$. Here, and in the following, the coordinate axes are along the two principal crystallographic directions of (110). For the (110) surfaces, the two principal directions are not equivalent to each other, and due to this, the constants $\lambda_{\alpha\beta}$ in Eq. (2.4) are generally unequal to each other. Thus, for (110) surfaces, there are five independent λ constants in Eq. (2.4). It is illuminating to note that for the higher symmetry (100) surfaces one has also the diagonal reflection symmetry [6] $(x_1, x_2) \to (x_2, x_1)$, implying $\lambda_{11} = \lambda_{22}$ and $\lambda_{12} = \lambda_{21}$ in Eq. (2.4). So, for the (100) surfaces, there are three independent λ constants in Eq. (2.4). Finally, for isotropic surfaces, Eq. (2.4) must be invariant under all 2D rotations, implying $\lambda_{11} = \lambda_{12} = \lambda_{21} = \lambda_{22} = \lambda_{\mathrm{VA}}$ and $\lambda_3 = 0$. In this case, Eq. (2.4) reduces to the conservative KPZ term of the simple (single constant) form

$$-\vec{\nabla} \cdot \vec{J}_{\mathrm{VA}} = -\frac{\lambda_{\mathrm{VA}}}{2} \nabla^2 (\vec{\nabla} h)^2, \tag{2.4'}$$

which is strictly applicable only to the idealized isotropic surfaces. The form of the nonequilibrium current $\vec{J}^{\mathrm{NE}}$ in Eq. (2.2) is also restricted by the reflection symmetries of the (110) surface, which imply the expansion of the form [4]

$$J_1^{\mathrm{NE}}(M_1, M_2) = M_1[r_1 - u_{11} M_1^2 - u_{12} M_2^2 + \cdots],$$

$$J_2^{\mathrm{NE}}(M_1, M_2) = M_2[r_2 - u_{22} M_2^2 - u_{21} M_1^2 + \cdots]. \tag{2.6}$$

The ellipses in Eq. (2.6) indicate higher order terms which will be truncated out in the following. This yields the simplest possible yet comprehensive model consistent with the symmetries of (110) surface which are respected by the terms exhibited explicitely in Eq. (2.6). By an anisotropic rescaling of the coordinates (x_1, x_2) discussed in Ref. [4] [see Eqs. (2.15) and (2.16) therein], the above continuum form of $\vec{J}^{\mathrm{NE}}$

can be made to depend only on three dimensionless parameters (a,b,c). In the rescaled model, $\vec{J}^{\rm NE}$ is as in Eq. (2.6) with $r_1=1+a$, $r_2=1-a$, $u_{11}=u_{22}=1$, $u_{12}=b+c$, $u_{21}=b-c$, as employed hereafter. Preferred interface slopes correspond to zeros of $\vec{J}^{\rm NE}(\vec{M})$. Thus, in the rescaled model, the R_1 doublet of facets (giving rise to the R_1 rippled state) occurs at the slopes

$$M_1 = \pm\sqrt{1+a}, \quad M_2 = 0. \tag{2.7}$$

Likewise, the R_2 doublet of facets (giving rise to the R_2 rippled state) occurs at the slopes

$$M_1 = 0, \quad M_2 = \pm\sqrt{1-a}. \tag{2.8}$$

Slopes in Eqs. (2.7) and (2.8) are shown in our Fig. 2(a). Importantly for our discussions, the R_1 and R_2 facets in Eqs. (2.7) and (2.8) are *both* stable for the parameter a in the range

$$a_+(b,c) < a < a_-(b,c) \tag{2.9}$$

with $a_+=(1-b+c)/(1+b-c)$ and $a_-=(1-b-c)/(1+b+c)$. For $a_+<a_-$, i.e., for $b>\sqrt{1+c^2}$, one has a multistable range Eq. (2.9) in which the rectangular rippled states $R_1^{(\rm rec)}$ and $R_2^{(\rm rec)}$ develop (see Ref. [4] and the discussions at beginning of Sec. III here). In this study, our primary interest is in the VA effects on the interface morphologies occurring in this multistable range. Unlike the simple rippled states, each of the two $R^{(\rm rec)}$ states involves both R_1 and R_2 facets; see Fig. 1. These two types of facets are not equivalent (symmetry related) to each other. Thus, in general, they can coexist only across moving edges between them [4]. Due to the edges motion, in the $R_1^{(\rm rec)}$ state, the R_1 facets grow faster than the R_2 facets, whereas in the $R_2^{(\rm rec)}$ state the R_2 facets grow faster than the R_1 facets. This edges motion produces the surface morphologies seen in rectangular rippled states; see Figs. 1(a) and 1(c). Only at a special (critical) point can one have a static edge between the R_1 and R_2 facets. For zero VA, this point occurs at $a=a_{\rm cr}$, with

$$a_{\rm cr} = \frac{\sqrt{1+(c/3)^2}-1}{c/3}, \tag{2.10}$$

see Ref. [4] and the discussion below Eq. (2.28) in the following. For $a=a_{\rm cr}$, the interface dynamics equation (2.1) has a steady solution

$$\frac{\partial h}{\partial t} = -\vec{\nabla}\cdot\vec{J}^{\rm NE} - \vec{\nabla}\cdot\vec{J}^{\rm curv} = 0, \tag{2.11}$$

corresponding to the static edge between semi-infinite R_1 and R_2 facets. For zero VA, the critical value of the control parameter a in Eq. (2.10) corresponds to the transition point between the $R_1^{(\rm rec)}$ and $R_2^{(\rm rec)}$ states [4]. At this critical point, R_1 and R_2 facets can coexist across the static edges. This feature allows for the nonequivalent R_1 and R_2 facets to grow at the same rate at the critical point. Thus, instead of rectangular rippled structures, one finds the checker-board structure of four sided pyramids; see Fig. 1(b) from our zero VA simulations at $a=a_{\rm cr}$. Thus, by this Gibbs' style argument (with the equilibrium Gibbs' interfaces between different phases corresponding to the static edges between nonequivalent facets), one can elucidate the kinetic phase transitions in epitaxial growth and erosion.

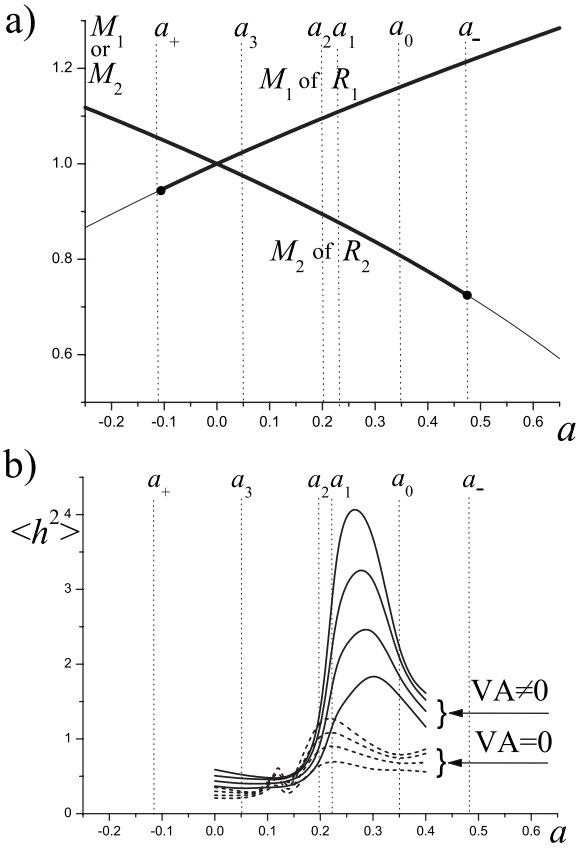

FIG. 2. Multistable range involved in the transition from the $R_2^{(\rm rec)}$ to $R_1^{(\rm rec)}$ state. a) Variations of the slopes of the R_1 and R_2 facets, respectively, $M_1=\sqrt{1+a}$ and $M_2=\sqrt{1-a}$, versus the temperaturelike dimensionless parameter a. Facet slopes are given by thick (thin) lines for stable (unstable) facets. Both R_1 and R_2 facets are stable for a in the range $a_+<a<a_-$. b) Variation of the square of the interface width $\langle h^2\rangle$, given (for nonzero VA) by solid lines for several different deposition times, versus the parameter a, as obtained from our simulations. Labeled are the four characteristic values of a, namely, $a_3<a_2<a_1<a_0$, discussed in the text. In these simulations, in Eq. (2.4) [so, in Eq. (3.1) as well] we set $\lambda_{11}=\lambda_{12}=\lambda_{21}=\lambda_{22}=\lambda$, and $\lambda_3=0$, as in the isotropic VA model, Eq. (2.4′), characterized by $\lambda''=0, \lambda=\lambda'$ [see the text after Eqs. (2.15) and (2.13)]. In Eq. (2.5) [so, in Eq. (3.1) as well], we set $\kappa_{11}=\kappa_{12}=\kappa_{22}=\kappa$, with $\lambda/\sqrt{\kappa}=3$ (see, also, Fig. 4 caption). Also, in Eq. (2.6), we set $c=3/4$ and $b=2$, yielding $a_+=-0.11$ and $a_-=0.47$ [see the text below Eq. (2.9)]. With these values, from our simulations we find the presence of four characteristic a parameter values $a_3\approx 0.05$, $a_2\approx 0.20$, $a_1\approx 0.225$, $a_0\approx 0.35$, discussed in Secs. II and III (see also Figs. 4–7). For comparison, in b) we include also the simulations results obtained with zero VA, i.e., $\lambda=0$ (dashed lines). The ripple rotation transition region occurs over a narrow range between $a_2\approx 0.2$ and $a_1\approx 0.225$; see also Fig. 5. Note that the VA significantly enhances interface roughness to the right of the ripple rotation transition region.

For nonzero VA, these far-from-equilibrium transitions can also be discussed by searching for the static edge solutions of the Eq. (2.11). However, with nonzero VA, an addi-

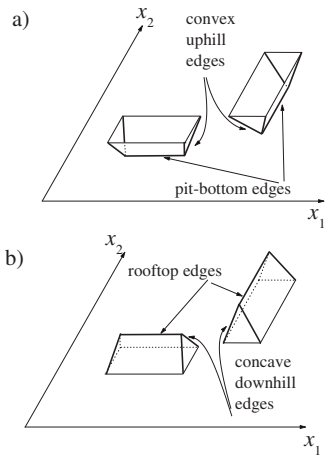

FIG. 3. a) Convex uphill edges between R_1 and R_2 facets. They emerge from the long edges along bottoms of rectangular shaped pits. For $a \neq a_{\text{convex}}$ the uphill edges move, so pits grow in length either along the x_1 direction (as in the $R_1^{(\text{rec})}$ state) or along x_2 direction (as in the $R_2^{(\text{rec})}$ state). b) Concave downhill edges between R_1 and R_2 facets. They emerge from the long edges along the rooftops of rectangular shaped pyramids. For $a \neq a_{\text{concave}}$, the downhill edges move, so rooftops grow in length either along the x_1 direction (as in the $R_1^{(\text{rec})}$ state) or along the x_2 direction (as in the $R_2^{(\text{rec})}$ state).

tional complexity emerges, because there are two distinct types of the edges between R_1 and R_2 facets, see Fig. 3: (i) the convex edges, such as the uphill edges emerging from the pit-bottom edges of the rectangular shaped pits of the $R^{(\text{rec})}$ state, see Fig. 3(a); (ii) the concave edges, such as the downhill edges emerging from the rooftop edges of the rectangular shaped pyramids of the $R^{(\text{rec})}$ state, see Fig. 3(b). For zero VA, these two types of static R_1-R_2 edges are simply related to each other, because if $+h(\vec{x})$ solves Eq. (2.11), then $-h(\vec{x})$ also solves the same equation. So, the static concave downhill edge is directly obtained from the static convex uphill edge, simply by the vertical reflection of the interface profile $h(\vec{x})$. Due to this, for zero VA, both types of static edges exist for the same critical value of the parameter a, given in Eq. (2.10). However, with ubiquitously present nonzero VA, the vertical reflection $h \to -h$ ceases to be a symmetry of the interface dynamics, i.e., if $+h(\vec{x})$ solves Eq. (2.11), then $-h(\vec{x})$ does not solve the same equation (for the same value of a). In view of this, for nonzero VA, the value of a needed for the existence of the static convex uphill edge [Fig. 3(a)] is generally different from the value of a needed for the existence of the static concave downhill edge [Fig. 3(b)]. Let us call these two special (critical) values of the control parameters as a_{convex} and a_{concave}. By the above discussions, in general,

$$a_{\text{convex}} \neq a_{\text{concave}}$$

unless VA is zero, hence a_{convex} and a_{concave} both become equal to the critical value given by Eq. (2.10). The existence of two distinct critical points will be shown in the following to be the major factor responsible for the complex VA induced interfacial morphologies revealed at the end of this section and in Sec. III.

We now proceed to discuss and extract a_{convex} and a_{concave} quantitatively, by solving Eq. (2.11) with nonzero VA. For this purpose, it is convenient to proceed by using a rotated coordinate system (x_T, x_L), with the x_T and x_L, respectively, perpendicular and along the edge. In this coordinate system, the interface profile for a very long static edge has the form

$$h(x_T, x_L) = M_L x_L + \Delta h(x_T), \tag{2.12}$$

where M_L=const is the longitudinal (L) slope component along the edge, whereas the function $\Delta h(x_T)$ can be found by solving Eq. (2.11). Note that

$$M_T(x_T) = \frac{\partial h}{\partial x_T} = \frac{d\Delta h(x_T)}{dx_T} \tag{2.13}$$

is simply the transversal (T) interface slope component (perpendicular to the edge). Unlike the constant M_L, the slope component $M_T(x_T)$ changes as one passes, for example, from the R_1 facet to the R_2 facet by going across the R_1-R_2 edge; see Fig. 4(a). For the static edge solution in Eq. (2.12), Eq. (2.11) [with entries given by Eqs. (2.4)–(2.6)] reduces to

$$0 = \frac{d}{dx_T} J_T(x_T) \tag{2.14}$$

with

$$J_T(x_T) = J_T^{\text{NE}}(M_T) + \kappa \frac{d^2 M_T}{dx_T^2} + \frac{1}{2}\lambda' \frac{d}{dx_T}(M_T)^2 - \lambda'' M_L \frac{d}{dx_T} M_T. \tag{2.15}$$

Here, J_T^{NE} is the $\vec{J}^{\text{NE}}$ component perpendicular to the edge, whereas (λ', λ'') and κ are, respectively, certain linear combinations of the λ and κ constants in Eqs. (2.4) and (2.5). For example, for the isotropic VA case, Eq. (2.4′), we find that $\lambda' = \lambda_{\text{VA}}$, $\lambda'' = 0$.

For $x_T \to \pm\infty$, the slope vector $\vec{M}$ approaches the R_1 and R_2 slope vectors at which $\vec{J}^{\text{NE}}(\vec{M})$ vanishes. Due to this, by invoking Eq. (2.14), $J_T(x_T)$ must be zero

$$J_T(x_T) = 0, \tag{2.16}$$

for a static edge interface profile. Finding it reduces to solving for $M_T(x_T)$ the nonlinear second order differential equation defined by Eqs. (2.16) and (2.15).

In the following, we discuss a_{convex} and a_{concave} for the R_1-R_2 edges between the R_1 and R_2 facets with the slope vectors given by Eqs. (2.7) and (2.8). Let us consider the R_1 facet with the slope vector $\vec{M}^{(R_1)} = (M_1 = \sqrt{1+a}, M_2 = 0)$, and the R_2 facet with the slope vector $\vec{M}^{(R_2)} = (M_1 = 0, M_2 = \sqrt{1-a})$, see Fig. 4(a). The above employed slope components (M_L, M_T) are related to the original slope vector (M_1, M_2) by the rotation

$$M_1 = M_L \cos(\psi) - M_T \sin(\psi),$$

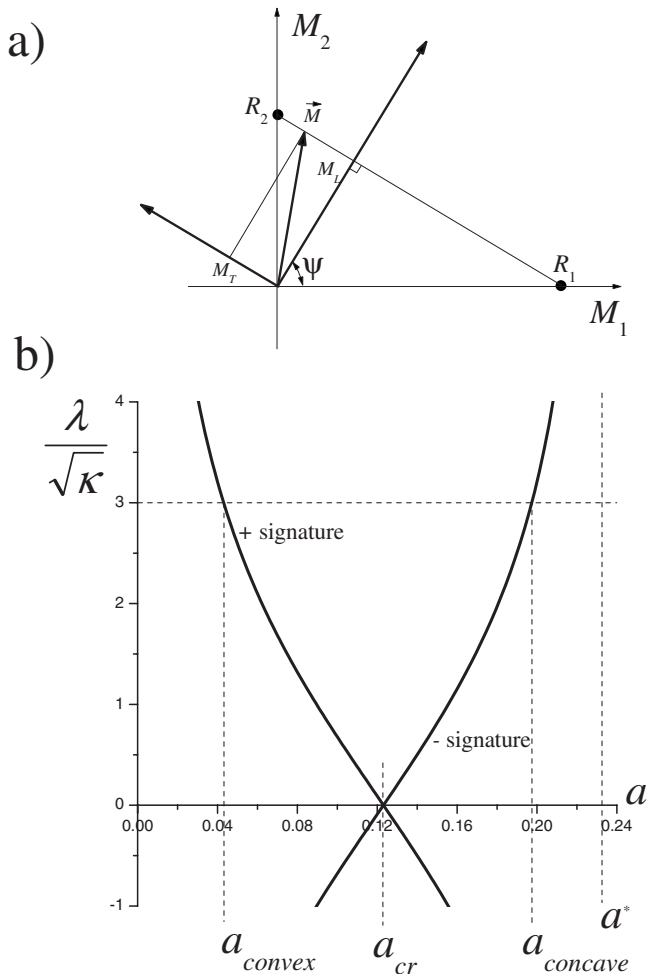

FIG. 4. a) aids the analytic discussions of Sec. II yielding the seminal condition Eq. (2.37) for the coexistence of the nonequivalent R_1 and R_2 facets across a static edge. b) plots Eq. (2.37) with both signatures. Here, as in our simulations, the graph is given for $c=3/4$, $b=2$, $\lambda'=\lambda$ as in the isotropic VA model Eq. (2.4′) hence Eq. (2.37) reduces to Eq. (2.37′); see Fig. 2 caption, and the text after Eqs. (2.15) and (2.31). For these values, $a_{cr}\cong 0.123$ by Eq. (2.10), whereas Eq. (2.37′) has a vertical asymptote seen at $a^*\cong 0.232$. For $\lambda/\sqrt{\kappa}=3$, as in the simulations, we find, by solving Eq. (2.37′), that $a_{convex}\cong 0.0431$ and $a_{concave}\cong 0.197$. These analytic results correspond accurately to the characteristic a parameter values $a_3\approx 0.05$ and $a_2\approx 0.20$ obtained from our simulations. Thus, the altered $R_2^{(rec)}$ state (with depressed pits) seen in the simulation in Fig. 5(b) actually occurs for the parameter a in the range $a_3=a_{convex}<a<a_2=a_{concave}$.

$$M_2 = M_L \sin(\psi) + M_T \cos(\psi), \tag{2.17}$$

where ψ is the rotation angle; $\sin(\psi)=\sqrt{(1+a)/2}$, $M_L=\sqrt{(1-a^2)/2}$, as easily deduced from Fig. 4(a). The transversal component of the current $\vec{J}^{NE}$ (along M_T) is

$$J_T^{NE} = J_2^{NE}\cos(\psi) - J_1^{NE}\sin(\psi). \tag{2.18}$$

Using Eqs. (2.18) and (2.17), in combination with Eq. (2.6), yields

$$J_T^{NE}(M_T) = -\beta(M_T - M_T^{(R_1)})(M_T - M_T^{(R_2)}) \times\left(M_T - \frac{M_T^{(R_1)} + M_T^{(R_2)}}{2} - \Delta M_T\right). \tag{2.19}$$

In Eq. (2.19),

$$M_T^{(R_1)} = -\frac{1+a}{\sqrt{2}}, \quad M_T^{(R_2)} = \frac{1-a}{\sqrt{2}}, \tag{2.20}$$

are the transversal components of the slope vectors of the R_1 and R_2 facets, whereas

$$\beta = 1 + \tfrac{1}{2}(1-a^2)(b-1) \tag{2.21}$$

and

$$\Delta M_T = \frac{6a - (1-a^2)c}{2\sqrt{2}\beta}. \tag{2.22}$$

To proceed, we change the variable $M_T(x_T)$ into

$$m(x_T) = M_T(x_T) - \frac{M_T^{(R_1)} + M_T^{(R_2)}}{2}. \tag{2.23}$$

With this change and by Eq. (2.19), our Eq. (2.16) assumes the form

$$0 = J_T(x_T) = j_1 + j_2 \tag{2.24}$$

with

$$j_1 = \beta m\left[\left(\frac{M_T^{(R_2)} - M_T^{(R_1)}}{2}\right)^2 - m^2\right] + \kappa\frac{d^2m}{dx_T^2} + \frac{\lambda'}{2}\frac{d}{dx_T}m^2 \tag{2.25}$$

and

$$j_2 = \beta\Delta M_T\left[\left(\frac{M_T^{(R_2)} - M_T^{(R_1)}}{2}\right)^2 - m^2\right] + \left(\lambda'\frac{M_T^{(R_1)} + M_T^{(R_2)}}{2} - \lambda'' M_L\right)\frac{d}{dx_T}m. \tag{2.26}$$

By Eq. (2.23),

$$M_T(x_T) - M_T^{(R_1)} = m_T(x_T) + \frac{M_T^{(R_2)} - M_T^{(R_1)}}{2},$$

$$M_T(x_T) - M_T^{(R_2)} = m_T(x_T) - \frac{M_T^{(R_2)} - M_T^{(R_1)}}{2}. \tag{2.27}$$

Note that, by Eq. (2.20), $(M_T^{(R_2)} - M_T^{(R_1)})/2 = 1/\sqrt{2}$ is a positive quantity here. By Eq. (2.27), there are two geometrically distinct edge solutions to Eq. (2.24): (i) *Convex static edges*. For them, $M_T(x_T)\to M_T^{(R_1)}$, i.e., $m(x_T)\to -(M_T^{(R_2)} - M_T^{(R_1)})/2$ for $x_T\to -\infty$, and $M_T(x_T)\to M_T^{(R_2)}$, i.e., $m(x_T)\to +(M_T^{(R_2)} - M_T^{(R_1)})/2$ for $x_T\to +\infty$. For convex edges, $M_T(x_T)$ is an increasing function of x_T, $dM_T/dx_T = \partial^2 h/\partial x_\perp^2 > 0$, justifying their name. (ii) *Concave static edges*. For them, $M_T(x_T)\to M_T^{(R_1)}$, i.e., $m(x_T)\to -(M_T^{(R_2)} - M_T^{(R_1)})/2$ for $x_T\to +\infty$, and $M_T(x_T)\to M_T^{(R_2)}$, i.e., $m(x_T)\to +(M_T^{(R_2)} - M_T^{(R_1)})/2$ for $x_T\to -\infty$. For concave edges, $M_T(x_T)$ is a decreasing function of

$x_T, dM_T/dx_T = \partial^2 h/\partial x_\perp^2 < 0$, justifying their name.

In terms of the order parameter $m(x_T)$, the static edges are thus expected to appear as topologically stable soliton type solutions to Eq. (2.24) similar to domain walls in magnetic systems [12]. However, by inspecting in detail the form of our Eqs. (2.24)–(2.26), the similarity to the familiar magnetic domain walls is manifest only for zero VA ($\lambda' = \lambda'' = 0$). In this limit, Eq. (2.24) can be shown to have domain-wall solutions that vanish both j_1 and j_2 separately. Indeed, the j_1 in Eq. (2.25) is easily shown to vanish for the domain wall solution of the form

$$m(x_T) = \pm \frac{M_T^{(R_2)} - M_T^{(R_1)}}{2} \tanh\left(\frac{x_T}{w_\pm}\right), \tag{2.28}$$

with (for zero VA) $w_+ = w_- = 2(\kappa_T/\beta)^{1/2}$, whereas, by Eq. (2.26) with zero VA, the condition $j_2 = 0$ then implies that $\Delta M_T = 0$. Using this and Eq. (2.22), we recover the zero VA critical value of the parameter $a_{\rm cr}$ stated in Eq. (2.10). In Eq. (2.28), the + (−) signature corresponds to convex (concave) edges. For zero VA, both convex and concave edges are realized at the same critical value of a, Eq. (2.10). This feature, as well as the equality of the convex and concave edges widths $w_+ = w_-$ is simply a consequence the "vertical symmetry" ($h \to -h$, i.e., $m \to -m$) acquired by the model and thus by Eq. (2.24) in the zero VA limit. However, the situation changes qualitatively for whatever nonzero VA. Convex and concave static edge solutions are then not related to each other by the vertical flip $m \to -m$. They are thus expected to have different profiles ($w_+ \neq w_-$). Even more interestingly, with a nonzero VA present, there is no any reason for convex and concave static edges to be realized at the same value of the system parameter a. Indeed, as discussed quantitatively hereafter, convex and concave static edges are realized at two different values of the system control parameter a, labeled as $a_{\rm convex}$ and $a_{\rm concave}$. A remarkable feature of our model, and of Eq. (2.24) with a nonzero VA, is that the static edges solutions can be (again) obtained in terms of exact analytic forms which vanish both j_1 and j_2 separately. Beyond this special and nontrivial feature is the following identity (a differential equation) satisfied by the standard tangent-hyperbolic function $y(z) = \tanh(z)$

$$\frac{dy}{dz} = 1 - y^2. \tag{2.29}$$

Applying this identity [and its consequence, $d(y^2/2)/dz = y(1-y^2)$] to the static edge profile of the form as in Eq. (2.28), one finds that j_1 in Eq. (2.25) assumes the form

$$j_1 = \frac{d}{dx_T}\left[\frac{m_0 \tanh^2(x_T/w)}{2w}[\beta(m_0 w)^2 + \lambda' m_0 w - 2\kappa]\right],$$

which implies that j_1 vanishes if the domain wall width w satisfies the equation

$$\beta(m_0 w)^2 + \lambda' m_0 w - 2\kappa = 0. \tag{2.30}$$

Above, $m_0 = \pm(M_T^{(R_2)} - M_T^{(R_1)})/2$, i.e., by Eq. (2.20), $m_0 = \pm 1/\sqrt{2}$, with + (−) signature corresponding to convex (concave) edges. Moreover, strikingly, by again using the identity Eq. (2.29), we find that j_2 in Eq. (2.26) also vanishes provided

$$\Delta M_T = \frac{\lambda'(M_T^{(R_1)} + M_T^{(R_2)}) - 2\lambda'' M_L}{2\beta m_0 w} = -\frac{\lambda a}{2^{1/2}\beta m_0 w}. \tag{2.31}$$

Here, $\lambda = \lambda' + \lambda''(1-a^2)^{1/2}/a$. In particular, for isotropic VA in Eq. (2.4′), $\lambda = \lambda'$ as $\lambda'' = 0$; see the text after Eq. (2.15).

Solving the quadratic Eq. (2.30) for $m_0 w$ yields

$$m_0 w = -\frac{\lambda'}{2\beta} \pm \sqrt{\left(\frac{\lambda'}{2\beta}\right)^2 + \frac{2\kappa}{\beta}}. \tag{2.32}$$

Here, the signature ± is to be chosen such that edge width $w > 0$ [we choose to regulate the overall sign of the solution Eq. (2.28) by the sign of the prefactor m_0 of the tanh function therein]. In view of this, the width of convex edges ($m_0 = +1/\sqrt{2} > 0$) is, by Eq. (2.32),

$$w_+ = \sqrt{2}\left(-\frac{\lambda'}{2\beta} + \sqrt{\left(\frac{\lambda'}{2\beta}\right)^2 + \frac{2\kappa}{\beta}}\right) > 0, \tag{2.33}$$

whereas the width of concave edges ($m_0 = -1/\sqrt{2} < 0$) is found as

$$w_- = \sqrt{2}\left(+\frac{\lambda'}{2\beta} + \sqrt{\left(\frac{\lambda'}{2\beta}\right)^2 + \frac{2\kappa}{\beta}}\right) > 0. \tag{2.34}$$

As anticipated before, these two distinct types of static edges are expected to be realized at two different critical values of the system parameter a, labeled as $a_{\rm convex}$ and $a_{\rm concave}$. To extract these values, we first solve Eq. (2.31) for $m_0 w$ and insert it into Eq. (2.30). This yields the equation

$$\frac{(\lambda)^2}{\beta\kappa} = \frac{\left(\frac{2\Delta M_T}{a}\right)^2}{1 - \sqrt{2}\frac{\lambda'}{\lambda}\frac{\Delta M_T}{a}}. \tag{2.35}$$

Next, note that by Eq. (2.31), the signs of the quantities entering Eq. (2.35) are related by $\mathrm{sgn}(\Delta M_T/a)\ \mathrm{sgn}(\lambda) = -\mathrm{sgn}(m_0)$. Using this, Eq. (2.35) is easily seen to be equivalent to

$$-\frac{\lambda}{\sqrt{\beta\kappa}} = \mathrm{sgn}(m_0)\frac{2\frac{\Delta M_T}{a}}{\sqrt{1 - \sqrt{2}\frac{\lambda'}{\lambda}\frac{\Delta M_T}{a}}}. \tag{2.36}$$

Using here Eqs. (2.21) and (2.22), we arrive at the equation

$$+\frac{\lambda}{\sqrt{\kappa}} = \pm \frac{-6 + (1-a^2)\frac{c}{a}}{\left[2 + (1-a^2)(b-1) + \frac{\lambda'}{\lambda}\left(-6 + (1-a^2)\frac{c}{a}\right)\right]^{1/2}}. \tag{2.37}$$

For example, for isotropic VA model in Eq. (2.4′), with $\lambda = \lambda'$ [as noted after Eq. (2.31)], Eq. (2.37) reduces to

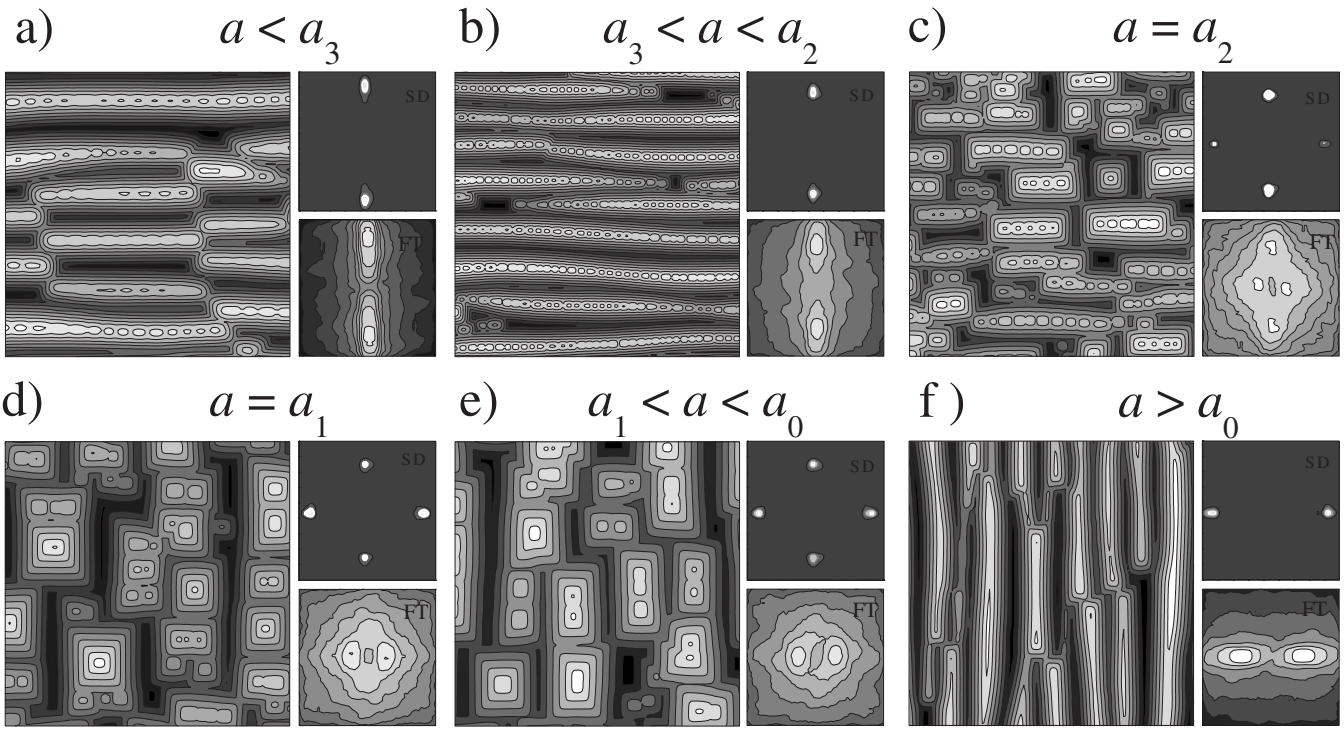

FIG. 5. Effects of the VA on the interface morphology (given here by surface contour plots) and interface diffraction data (SD and FT), across the transition from $R_2^{(\mathrm{rec})}$ to $R_1^{(\mathrm{rec})}$ state. a) The $R_2^{(\mathrm{rec})}$ state, with a checkerboard arrangement of rectangular elongated pyramids and pits (inverted rooftops). b) Altered form of $R_2^{(\mathrm{rec})}$ state (wormlike ripples): the pit sizes are depressed and that arrays of small rounded mounds form along rooftops of elongated pyramids. c) Interface morphology at the point where surface FT exhibits four peaks of equal magnitude (four-lobe pattern) corresponds to rectangular mounds packed side-by-side. d) Interface morphology at the point where surface SD exhibits four peaks of equal magnitude. e) Altered form of the $R_1^{(\mathrm{rec})}$ state (square pyramidlike state): rooftoplike pyramids replaced by arrays of nearly square shaped four-sided pyramids packed between longer in size pits (inverted rooftops). f) The $R_1^{(\mathrm{rec})}$ state, with a checkerboard arrangement of rectangular elongated pyramids and pits (inverted rooftops).

$$+\frac{\lambda}{\sqrt{\kappa}} = \pm \frac{-6 + (1-a^2)\dfrac{c}{a}}{\left[-4 + (1-a^2)\left(b - 1 + \dfrac{c}{a}\right)\right]^{1/2}}. \quad (2.37')$$

In Eqs. (2.37) and (2.37′), the + signature corresponds to convex edges (with $m_0 = +1/\sqrt{2} > 0$) whereas the − signature corresponds to the concave edges (with $m_0 = -1/\sqrt{2} < 0$). Equation (2.37) is our central analytic result and the key for understanding phenomena revealed by numerical simulation discussed in the following. For given λ, i.e., for a given strength of the VA, Eq. (2.37) can be applied with the + signature to find a_{convex}, and with the − signature to find a_{concave}, as illustrated in Fig. 4(b). For zero VA ($\lambda = 0$), Eq. (2.37) yields the single critical value a_{cr} in Eq. (2.10), which vanishes the numerator on the right-hand side of Eq. (2.37). For this case only, obviously by the form of Eq. (2.37), the signature does not matter, so $a_{\mathrm{convex}} = a_{\mathrm{concave}} = a_{\mathrm{cr}}$. However, for any $\lambda \neq 0$, solving Eq. (2.37) for a gives a distinct a value for each signature, a_{convex} with − signature, and a_{concave} with + signature, as evident from Fig. 4(b). It plots the Eq. (2.37), with both signatures. From Fig. 4(b), we see that, for a positive VA, i.e., $\lambda > 0$ (what is likely typical situation in epitaxial growth and erosion [11]) one has

$$a_{\mathrm{convex}} < a_{\mathrm{concave}}. \quad (2.38)$$

To elucidate full meaning and implications of a_{convex} and a_{concave} on interface morphology, we carried out extensive numerical simulations of our model in Eqs. (2.1) through (2.6). These simulations reveal the existence of four characteristic a parameter values $a_3 < a_2 < a_1 < a_0$ related to VA; see Figs. 2, 5, and 6. The very ripple rotation transition occurs in a narrow range between a_2 and a_1; see Sec. III. Quantitative comparisons between the solutions to Eq. (2.37) and our simulations, reveal that $a_{\mathrm{convex}} \approx a_3$ and $a_{\mathrm{concave}} \approx a_2 \approx a_1$; see Fig. 4 caption. By Eq. (2.38), by decreasing the control parameter a, the system first encounters a_{concave}, at which the concave downhill edges [emerging from the rooftops of the $R_1^{(\mathrm{rec})}$ state rectangular pyramids, see Fig. 3(b)] become static. By a further decrease of a, the system encounters a_{convex}, at which the convex uphill edges [emerging from the bottoms of the $R_2^{(\mathrm{rec})}$ rectangular pits, see Fig. 3(a)] become static. Because of these features, several qualitatively different interface morphologies are encountered with decreasing the control parameter a.

(i) For a sufficiently above $a_{\mathrm{concave}} (> a_{\mathrm{convex}})$, both the rooftops and pit bottoms grow along the x_2 direction [much as for zero VA in Fig. 1(c)]. Thus, the interface is in the $R_1^{(\mathrm{rec})}$ state, if a is sufficiently above a_{concave}, as seen in our simulations for $a > a_0 (> a_{\mathrm{concave}})$ in Fig. 5(f).

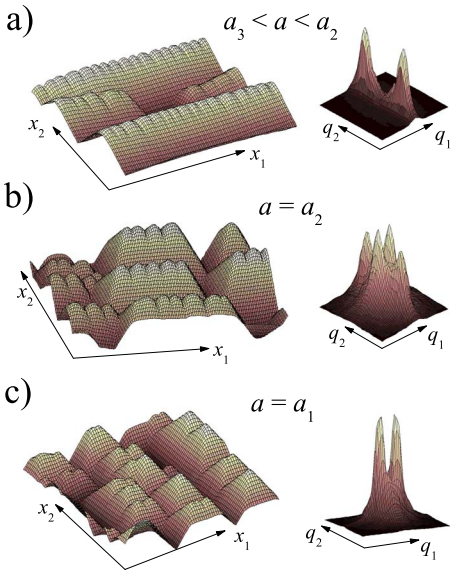

FIG. 6. (Color online) 3D views of the real-space interface morphology and the corresponding FTs, i.e., near in-phase diffraction patterns, for a nonzero VA, at several successive points along the ripple rotation transition between the rectangular rippled states. In a), the altered form of the $R_2^{(\mathrm{rec})}$ state is shown. In it, pits sizes are depressed whereas arrays of small mounds form along rooftops. Note that this structure yields a FT which is essentially the same as that of the $R_2^{(\mathrm{rec})}$ state, with just two peaks at $(0,\pm q_2)$ [see, also, Figs. 5(a) and 5(b)]. In b), the FT forms with two pairs of peaks, at $(\pm q_1,0)$ and $(0,\pm q_2)$, having nearly equal magnitudes (four-lobe pattern). This corresponds to the transition at $a=a_2$ discussed in our text and seen on Ag(110) in Ref. [1]. At it, the interface structures itself into rectangular pyramids sitting side-by-side [see also Fig. 5(c)]. In c), the altered form of the $R_1^{(\mathrm{rec})}$ state is shown, with rooftop edges replaced by arrays of nearly square shaped four-sided pyramids [see also Figs. 5(d) and 5(e)]. Nonetheless, this complex structure has qualitatively the same FT as $R_1^{(\mathrm{rec})}$, with just two peaks at $(\pm q_1,0)$ [see, also, Figs. 5(d)–5(f)].

(ii) For $a \approx a_{\mathrm{concave}} (> a_{\mathrm{convex}})$, the concave downhill edges [emerging from rooftops, see Fig. 3(b)] become nearly static by the above analytic discussions. This feature hinders the growth of rooftops in an a range above a_1 and below of a_0, but (as $a > a_{\mathrm{convex}}$), the pits are still prone to grow in length. This is exactly the situation we see from our simulations in Fig. 5(e), for a in the range $a_1 < a < a_0$, evidencing the growth of long pits and, also, the fact that long rectangular rooftops cease to develop. Rather, they break into arrays of small four sided pyramids seen in Fig. 5(e). This altered form of the $R_1^{(\mathrm{rec})}$ state seen in Fig. 5(e) for a in the range $a_1 < a < a_0$, is discussed in more details in Sec. III.

(iii) For $a \approx a_{\mathrm{convex}} (< a_{\mathrm{concave}})$ the convex uphill edges [emerging from pit bottoms, see Fig. 3(a)] become nearly static by the above analytic discussions. This feature hinders the growth of pits, but (as $a < a_{\mathrm{concave}}$), the rooftops are prone to grow in length. This is exactly the situation we see from our simulations in Fig. 5(b), for a in the range $a_3 < a < a_2$, evidencing the growth of long rooftops and also, the fact that pit bottoms are depressed in size and do not substantially grow in time. This altered form of the $R_2^{(\mathrm{rec})}$ state in Fig. 5(b), for a in the range $a_3 \approx a_{\mathrm{convex}} < a < a_2 \approx a_{\mathrm{concave}}$, is discussed in detail in Sec. III.

(iv) For a below $a_{\mathrm{convex}} (< a_{\mathrm{concave}})$, both the rooftops and pit bottoms grow along the x_1 direction [much as for zero VA in Fig. 1(a)]. Thus, the interface is in the $R_2^{(\mathrm{rec})}$ state, if a is below a_{convex}, as seen in our simulations for $a < a_3 \approx a_{\mathrm{convex}}$ in Fig. 5(a).

Notably, beyond the above multitude of interfacial states is the presence of ubiquitous vertical asymmetry. The VA differently affects the concave uphill edges and concave downhill edges. They become static at two distinct values of the system control parameter a_{convex} and a_{concave}. This VA effect gives rise to a complex kinetic phase diagram suggested by our simulations in Fig. 5. In addition to the rectangular rippled states $R_1^{(\mathrm{rec})}$ [Fig. 5(f)] and $R_2^{(\mathrm{rec})}$ [Fig. 5(a)], the phase diagram involves two VA induced interface states: the altered $R_1^{(\mathrm{rec})}$ state [Fig. 5(e)] and the altered $R_2^{(\mathrm{rec})}$ state [Fig. 5(b)]. Note that the ripple rotation transition actually proceeds as a transition between the two altered rectangular states. The transition and the altered rippled rectangular states are discussed in more detail in Sec. III.

III. RIPPLE ROTATION TRANSITION AND ALTERED RECTANGULAR RIPPLED STATES

In this section, we continue discussions of our numerical simulations of the model in Eqs. (2.1) through (2.6). Combining these equations yields interface height evolution equation

$$\begin{aligned}\frac{\partial h}{\partial t} = &- \frac{\partial}{\partial x_1}\left\{\frac{\partial h}{\partial x_1}\left[r_1 - u_{11}\left(\frac{\partial h}{\partial x_1}\right)^2 - u_{12}\left(\frac{\partial h}{\partial x_2}\right)^2\right]\right\} \\ &- \frac{\partial}{\partial x_2}\left\{\frac{\partial h}{\partial x_2}\left[r_2 - u_{22}\left(\frac{\partial h}{\partial x_2}\right)^2 - u_{21}\left(\frac{\partial h}{\partial x_1}\right)^2\right]\right\} \\ &- \kappa_{11}\left(\frac{\partial}{\partial x_1}\right)^4 h - 2\kappa_{12}\left(\frac{\partial}{\partial x_1}\right)^2\left(\frac{\partial}{\partial x_2}\right)^2 h - \kappa_{22}\left(\frac{\partial}{\partial x_2}\right)^4 h \\ &- \frac{\lambda_{11}}{2}\left(\frac{\partial}{\partial x_1}\right)^2\left(\frac{\partial h}{\partial x_1}\right)^2 - \frac{\lambda_{12}}{2}\left(\frac{\partial}{\partial x_1}\right)^2\left(\frac{\partial h}{\partial x_2}\right)^2 \\ &- \frac{\lambda_{21}}{2}\left(\frac{\partial}{\partial x_2}\right)^2\left(\frac{\partial h}{\partial x_1}\right)^2 - \frac{\lambda_{22}}{2}\left(\frac{\partial}{\partial x_2}\right)^2\left(\frac{\partial h}{\partial x_2}\right)^2 \\ &- \frac{\lambda_3}{2}\frac{\partial}{\partial x_1}\frac{\partial}{\partial x_2}\left[\frac{\partial h}{\partial x_1}\frac{\partial h}{\partial x_2}\right]. \end{aligned} \tag{3.1}$$

We solved the above interface evolution equation numerically by standard Euler algorithm, with finite differences approximating spatial derivatives as they stand in Eq. (3.1), to preserve the volume conservation law. We employed the standard initial condition with $h(x_1,x_2,t=0)=0+$small random number [different at each grid site (x_1,x_2)]. This corresponds to nearly horizontal interface, close to the unstable $h=0$ interface configuration. For other details of our simulations, see the caption of Fig. 2. We stress that there are no noise terms in Eq. (3.1). Thus, the ultimate (long times) interface morphologies depend only on the values of model parameters. As noted in Sec. II, by a simple anisotropic res-

caling of the coordinates (x_1,x_2), the continuum model Eq. (3.1) can be made to depend on three dimensionless parameters (a,b,c); see Ref. [4] and Eqs. (2.15) and (2.16) therein. In the rescaled model, interface dynamics equation is as in Eq. (3.1) above, with $r_1=1+a$, $r_2=1-a$, $u_{11}=u_{22}=1$, $u_{12}=b+c$, $u_{21}=b-c$, as employed in Ref. [4] and throughout this paper as well. As discussed in detail in Ref. [4], the phenomenological parameter a is directly related to the experimental control parameter (temperature, deposition, erosion flux, etc.) the change of which produces the ripple rotation transition, from the ripples oriented along x_1 direction to the ripples oriented along the x_2. This property of the parameter a is a basic mathematical feature embedded in our continuum model [4]. On the other hand, comparisons of the phenomenological theory in Ref. [4] with the experiments on various (110) surfaces show that the parameters b and c do not significantly depend on the experimental control parameter producing the ripple rotation transition. Rather, b and c are more materials dependent: Some materials (such as Ag; see Refs. [1,2]) exhibit the ripple rotation transition involving our rectangular rippled states (this scenario is realized if $b>\sqrt{1+c^2}$ in our model), whereas other materials (such as Cu and Rh; see the works under Ref. [3]) exhibit the ripple rotation transition involving our rhomboidal pyramid state (this scenario is realized if $b<\sqrt{1+c^2}$ in our model). In this study, our primary interest is in the VA effects on the interface morphologies occurring for $b>\sqrt{1+c^2}$, i.e., in the materials such as Ag, in which the ripple rotation transition involves the formation of rectangular rippled states.

The results of the simulations to be presented in this section reveal that the VA is essential for elucidating the experiments that have reported the ripple rotation transition on the Ag(110) crystal surface [1,2]. Within our model, as in the homoepitaxial growth experiments on the Ag(110) [1], the transition occurs within a multistable system parameter range in which R_1 and R_2 facets are both stable. The slopes of these facets, as obtained from our model, are depicted in Fig. 2(a) versus the control parameter a. The facets slopes and facet multistability behaviors seen in our Fig. 2(a) are in a remarkable qualitative agreement with the facets multistability behaviors seen on Ag(110) with changing substrate temperature [see Fig. 3(a) of Ref. [1]], provided our a is identified as a temperaturelike control parameter. As discussed in Sec. II, the VA current is a curvature current vanishing on flat facets. Thus, the VA does not affect the magnitudes of the selected slopes of the flat facets R_1 and R_2. They are determined purely by the form of the nonequilibrium current yielding Eqs. (2.6) and (2.7) depicted in Fig. 2(a). Nonetheless, the VA does qualitatively affect the long length scale interface morphology in an ample range around the transition. Compare our Fig. 5 obtained with a nonzero VA, with the Fig. 1 obtained with zero VA. As detailed hereafter, the experimental data of Refs. [1,2] are in accord with the predictions coming from our theory provided the VA is incorporated into the modeling. Practically significant among these data are the experimentally obtained in Ref. [1] surface diffraction patterns, i.e., the near in-phase and out-of-phase diffraction patterns corresponding, respectively, to the surface Fourier transform (FT) magnitude and slope distribution (SD) obtained from our simulations. Here, we will show that various experimental data on Ag(110) growth [1] and erosion [2] can be physically elucidated only if nonzero VA is incorporated into the theoretical picture.

We begin by discussing the a parameter range $a_2<a<a_1$. Therein, in Fig. 2(b) we see a sharp increase of the interface roughness. It is accompanied by nontrivial changes of the surface data such as its FT, i.e., the near in-phase diffraction pattern which exhibits four equally strong peaks for $a=a_2$ [see Fig. 5(c)] and, also, the changes of the surface SD, i.e., out-of-phase diffraction pattern which exhibits four equally peaks for $a=a_1$ [see Fig. 5(d)], close to the roughness maximum seen in Fig. 2(b). As evidenced in Fig. 5, for $a<a_1$, the character of both types of diffraction data (SD and FT) is closer to that of the $R_2^{(\mathrm{rec})}$ state, whereas, for $a>a_2$, it is closer to that of the $R_1^{(\mathrm{rec})}$ state. Thus, in terms of the standard diffraction data, the ripple rotation transition actually occurs over an extended parameter range $a_2<a<a_1$, which is narrow and characterized by a very steep rise of the interface roughness that actually occurs between a_2 and a_1, see Fig. 2(b). From the comparisons presented in Fig. 2(b), we see that VA strongly enhances the interface roughness yielding the prominent peak of the interface width seen across the transition. Interestingly, for $a=a_1$, close to the point corresponding to the maximum roughness (growing there as $\langle h^2\rangle^{1/2}\sim t^{0.5}$), the interface structures itself into nearly squarelike pyramids that are arranged side-by-side, see Figs. 5(d) and 6(c). We stress that such enhanced surface roughening has been indeed seen in the ripple rotation transition on Ag(110), in the epitaxial erosion experiments of Ref. [2]. Moreover, in the STM images from these experiments, one can see side-by-side arranged square pyramids as in our Fig. 5(d) [see Fig. 4(c) of Ref. [2]]. Strikingly, we find that the ripple rotation proceeds as a sequence of two experimentally significant (for the diffraction surface probes) transitions that we find in the proximity of the surface roughness maximum. The first of them, at $a=a_1$, occurs close to the point of maximum roughness. This transition is experimentally detectable by means of SD which for $a=a_1$ exhibits two equally strong pairs of peaks: the R_1 peaks at the slopes $(\pm M_1,0)$ and the R_2 peaks at the slopes $(0,\pm M_2)$, as seen in Fig. 5(d). At this transition point, interface structures itself into nearly square shaped pyramids sitting side-by-side, as evidenced by Figs. 5(d) and 6(c). Note that these squarelike pyramids form arrays that are packed between long pits (inverted rooftops). Interestingly, the presences of the long pits conspires to produce the interface FT seen at $a=a_1$ [Figs. 5(d) and 6(c)] which is qualitatively the same as that of rippled rectangular state $R_1^{(\mathrm{rec})}$ [Figs. 5(f)]. Thus, this first transition point, at $a=a_1$, can be seen *only* through SD data exhibiting the four equally strong peaks seen in Fig. 5(d). On the other hand, the FT data undergo a qualitative change at another phase transition point, at $a=a_2$, off the point with maximum roughness; see Figs. 2(b) and 5(c). At this transition, the near in-phase diffraction pattern, i.e., interface FT magnitude plot exhibits two equally strong pairs of peaks seen in Figs. 5(c) and 6(b): the R_1-state-like peaks at $(\pm q_1,0)$ and the R_2-state-like peaks at $(0,\pm q_2)$. Such a four-lobe near in-phase diffraction pattern has been indeed seen in the ripple rotation transition on Ag(110) surface [1]. At this tran-

sition point, we find that the surface structures itself into rectangular pyramids sitting side by side; see Figs. 5(c) and 6(b), both at $a=a_2$. We stress that for zero VA, at the very $R_1^{(\mathrm{rec})}$-to-$R_2^{(\mathrm{rec})}$ transition the interface has the FT with four peaks at the wave vectors $(\pm q_1, \pm q_2)$, see Fig. 1(b) here [4]. This is in striking contrast to our theoretical results with nonzero VA in Figs. 5(c) and 6(b) which are in full accord with the experiments on the Ag(110) growth [1], indicating a FT pattern with two pairs of peaks $(\pm q_1, 0)$ and $(0, \pm q_2)$ that are along the principal axes of the (110) surface. Thus, the incorporation of VA is essential in order to reproduce the four-lobe experimental diffraction pattern of Ref. [1]. This fact provides rigorous evidence showing that VA plays a significant role in epitaxial growth and erosion on crystal surfaces.

Our simulations in Fig. 5 reveal the existence of two VA induced surface morphologies called in Sec. II "altered rectangular rippled" states, the Alt$R_1^{(\mathrm{rec})}$ and Alt$R_2^{(\mathrm{rec})}$ seen in Figs. 5(e) and 5(b), respectively. By Fig. 5, the ripple rotation transition actually proceeds as a transition between the two altered rectangular states. For the parameter a in the range $a_3<a<a_2$ in Fig. 2, we find the Alt$R_2^{(\mathrm{rec})}$ state [Figs. 5(b) and 6(a)] which is the altered form of the $R_2^{(\mathrm{rec})}$ rippled state [Fig. 5(a)]. Prominent difference between the $R_2^{(\mathrm{rec})}$ and Alt$R_2^{(\mathrm{rec})}$ states is in the behavior of their pits. In the $R_2^{(\mathrm{rec})}$ state, the rectangular pyramids (roof tops) and the rectangular pits (inverted roof tops) grow with the same length [both with and without VA; see Figs. 5(a) and 1(a)]. In contrast to this, in the Alt$R_2^{(\mathrm{rec})}$ state, the rectangular pits remain small while the elongated pyramids grow in time, as seen in Figs. 5(b) and 6(a). In spite of this marked morphological feature, the Alt$R_2^{(\mathrm{rec})}$ state has both the near in-phase and out-of-phase diffraction patterns practically indistinguishable from those of the $R_2^{(\mathrm{rec})}$ state [compare Fig. 5(b) with Fig. 5(a)]. A direct (real space) probes of the interface, e.g., STM images, are thus needed to experimentally distinguish between the $R_2^{(\mathrm{rec})}$ and Alt$R_2^{(\mathrm{rec})}$ states. Interestingly, VA induces an instability of the rooftop edges on the elongated pyramids seen in Figs. 5(b) and 6(a) in the Alt$R_2^{(\mathrm{rec})}$ state and, also, in a range of the $R_2^{(\mathrm{rec})}$ state [see Fig. 5(a)]. There, we see that the rooftop edges are actually decorated by arrays of small rounded mounds. These mounds are, however, small in size and thus do not affect the interface diffraction data seen in Figs. 5(a) and 5(b), which are qualitatively the same as for zero VA [see Fig. 1(a)]. A direct look at the interface, by means of STM images, is thus needed to see these arrays of small mounds in the experiments. In Figs. 5(a) and 5(b), these arrays of small mounds are seen to develop only on the rooftops of the elongated pyramids whereas there are no such arrays developing along the pits. Importantly, the Alt$R_2^{(\mathrm{rec})}$ state does *not* exhibit an enhanced roughening [see Fig. 2(b)]. As in the $R_2^{(\mathrm{rec})}$ state [4], the interface roughness in the Alt$R_2^{(\mathrm{rec})}$ state grows as $\langle h^2\rangle^{1/2} \sim t^{1/4}$.

On the other side of the ripple rotation transition, with the a parameter in the range $a_1<a<a_0$ in Fig. 2, we have Alt$R_1^{(\mathrm{rec})}$ state seen in Fig. 5(e). This is an intensely rough state with its interface roughness growing as $\langle h^2\rangle^{1/2} \sim t^{0.4}$. The Alt$R_1^{(\mathrm{rec})}$ state near in-phase and out-of-phase diffraction data in Fig. 5(e) are nearly the same as those of the $R_1^{(\mathrm{rec})}$ state in Fig. 5(f). Yet, in the real space STM images, this intensely rough Alt$R_1^{(\mathrm{rec})}$ state would resemble a square-pyramid structured interface, with the pyramids sitting side-by-side, as seen in Fig. 5(e). Strikingly, however, a careful look at the interface in Fig. 5(e) shows that the intensely rough state has the long length-scale organization of the $R_1^{(\mathrm{rec})}$ state [seen in Fig. 5(f)], however, with long rooflike rectangular mounds replaced by arrays of small four-sided pyramids packed between long rectangular pits. Due to this feature, the state in Fig. 5(e) exhibits diffraction patterns which are nearly the same as those of the rectangular rippled state $R_1^{(\mathrm{rec})}$ [Fig. 5(f)]. Thus, the real space STM images are needed to discriminate this intensely rough $R_1^{(\mathrm{rec})}$ state seen in Fig. 5(e), from the $R_1^{(\mathrm{rec})}$ state seen in Fig. 5(f).

IV. SUMMARY AND DISCUSSION OF EXPERIMENTS

Here we summarize our theoretical results and compare them with the experimental STM data of Ref. [2] [ion beam erosion of Ag(110)] and the diffraction data of Ref. [1] [epitaxial growth on Ag(110)]. In both experiments, the system control parameter used was the substrate temperature. In the following we relate the experimentally observed data to the wealth of interfacial phenomena in our Figs. 5 and 6 that are produced by VA on (110) crystal surfaces in the ripple rotation transition involving the rectangular rippled states $R_1^{(\mathrm{rec})}$ and $R_2^{(\mathrm{rec})}$. Across this transition, with the change of the temperaturelike parameter a, there is number of interesting transitions occurring at the six characteristic points $a_+<a_3<a_2<a_1<a_0<a_-$, see Fig. 7(b). (i) In the range $a<a_+$, the rippled state R_2 occurs (not shown here, see Ref. [4]). (ii) In the range $a_+<a<a_3$, the $R_2^{(\mathrm{rec})}$ state occurs [see Fig. 5(a)]. (iii) In the range $a_3<a<a_2$, our Alt$R_2^{(\mathrm{rec})}$ occurs, with depressed pit sizes and with rooftop edges decorated by arrays of small rounded mounds. Still, all standard diffraction data of this state are the same as those of the $R_2^{(\mathrm{rec})}$ state [Figs. 5(b) and 6(a)]. The elongated pyramids of the Alt$R_2^{(\mathrm{rec})}$ state have wormlike shapes. Such a wormlike morphology of ripples has been indeed seen in the STM image in Fig. 4(b) of Ref. [2], which nicely parallels our Fig. 5(b). This state morphology can be described as being obtained by cutting an infinitely long worm into segments. The "cutting" is provided by the small pits placed between the long segments as seen in our Fig. 5(b), in accord with the STM image in Fig. 4(b) of Ref. [2]. In addition, in the same STM image one can see also a modulation of the widths of wormlike pyramids (pearl-like substructure), corresponding to the presence of the arrays of small rounded mounds in Fig. 5(b). (iv) At $a \approx a_2$, the interface structures itself as rectangular mounds sitting side-by-side, and the in-phase diffraction pattern exhibits two equally strong pairs of peaks, at $(\pm q_1, 0)$ and $(0, \pm q_2)$ as seen in Figs. 5(c) and 6(b). This corresponds to the four-lobe near in-phase diffraction pattern observed in Ref. [1] at the ripple rotation transition on Ag(110). We recall that there is no such FT interface pattern present with zero VA; see Fig. 1(b) in which the four-lobe FT pattern has peak positions different from those seen both in the experiments

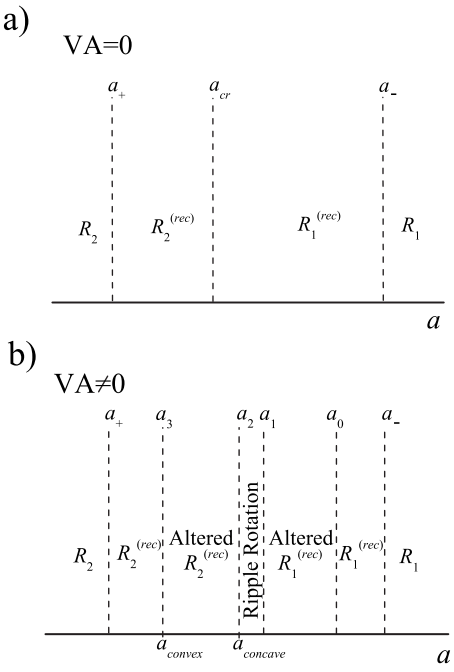

FIG. 7. Kinetic phase diagram of the growing (110) interface for zero VA a), and for nonzero VA b). Note that VA introduces two new interfacial states, the altered $R_1^{(\mathrm{rec})}$ state and the altered $R_2^{(\mathrm{rec})}$ state. Also, VA causes a smearing of the ripple rotation transition over extended parameter range (a_2,a_1). For VA$\rightarrow$0, the range of the altered states (a_3,a_0) in b), shrinks to a single critical point, a_{cr} in a). In b), $a_{\mathrm{convex}} \approx a_3$ and $a_{\mathrm{concave}} \approx a_2$ label the values of the control parameter a for which, respectively, static convex uphill edges [Fig. 3(a)] and static concave downhill edges [Fig. 3(b)] exist. As VA$\rightarrow$0, a_{convex} and a_{concave} in b) merge into a single critical point a_{cr} in a).

[1] and in our simulations in Figs. 5(c) and 6(b) with nonzero VA. Thus, our theoretical findings with nonzero VA, in combination with the experiments [1], provide rigorous evidence that VA plays a significant qualitative role in epitaxial growth and erosion on crystal surfaces. Our results demonstrate the VA's ability to induce formation of unique interface morphologies different from those that would occur with zero VA; compare Figs. 5(c) and 1(b). (v) The range $a_2<a<a_1$, characterized by a steep increase of the interface roughness in Fig. 2(b), is an extended ripple rotation transition region inside of which the interface SD (out-of-phase diffraction pattern) is more like to that of $R_2^{(\mathrm{rec})}$ state, whereas the interface FT (the in-phase diffraction pattern) is more similar to that of the $R_1^{(\mathrm{rec})}$ state. (vi) At $a \approx a_1$, the interface SD, i.e., out-of-phase diffraction pattern has two equally strong peaks, at $(\pm M_1,0)$ and $(0,\pm M_2)$ seen in Fig. 5(d). (vii) For a in the range $a_1<a<a_0$, the Alt$R_1^{(\mathrm{rec})}$ state occurs. It exhibits enhanced roughening seen in Fig. 2(b), and it is characterized by rooftop edges replaced by arrays of small nearly square shaped pyramids packed between long pits seen in Fig. 5(e). Due to this, all diffraction data of the intensely rough Alt$R_1^{(\mathrm{rec})}$ state are nearly the same as those of the $R_1^{(\mathrm{rec})}$ state that occurs for $a>a_0$ in Fig. 5(f). Such an intensely rough state has been indeed seen in the ripple rotation transition of Ag(110) in the epitaxial erosion experiments [2]. In fact, in the STM image in Fig. 4(c) of Ref. [2], one can indeed see side-by-side arranged nearly square shaped pyramids of our Alt$R_1^{(\mathrm{rec})}$ state in Fig. 5(e). (viii) Just next to this STM image of Ref. [2] one can furthermore see rectangular pyramids of our $R_1^{(\mathrm{rec})}$ state $(a_0<a<a)$, with our Fig. 5(f) corresponding to the STM image in Fig. 4(d) of Ref. [2]. This state is checkerboard arrangement of rectangular elongated pyramids and pits (inverted rooftops). (ix) Finally, in the range $a>a_-$, the rippled state R_1 occurs (not shown here, see Ref. [4]). It corresponds to the STM image in Fig. 4(e) of Ref. [2], which nicely illustrates the presence of rippled state dislocations theoretically discussed in Ref. [4].

In addition to the above agreements between our theory and the experimental surface morphology data on Ag(110) [1,2], there is also a remarkable agreement with the surface roughness and feature size data measured across the ripple rotation transition [2]. Experimentally, these data are highly asymmetric across the transition [2], in accord with our simulations results in Fig. 2(b). Our study has elucidated this asymmetry in terms of the difference between the roughening characters of the wormlike altered $R_2^{(\mathrm{rec})}$ state in Fig. 5(b), with the surface roughness $\sim t^{0.25}$, and significantly rougher square pyramidlike altered $R_1^{(\mathrm{rec})}$ state in Fig. 5(e), with the roughness $\sim t^{0.4}$. Multitude of interfacial phenomena revealed in this study is summarized in Fig. 7 in which, for comparison, we depict kinetic phase diagram forms both without [Fig. 7(a)] and with VA [Fig. 7(b)]. The comparison well illustrates qualitatively significant effects induced by the VA. Vertical asymmetry changes qualitatively the morphology of the standard rectangular rippled states in the proximity of the ripple rotation transition. Two new types of interfacial states, the altered $R_1^{(\mathrm{rec})}$ state and the altered $R_2^{(\mathrm{rec})}$ state, emerge in Fig. 7(b), purely due to the VA. Importantly, the very ripple rotation itself goes on as a transition between the two altered rectangular rippled states. Due to VA, the transition occurs over an extended parameter range interposed between the altered states ranges. For VA$\rightarrow$0, the ranges of the altered $R_1^{(\mathrm{rec})}$ and altered $R_2^{(\mathrm{rec})}$ states, and ripple rotation transition range, all shrink to a single critical point, the a_{cr} in Fig. 7(a). For zero VA, a_{cr} was identified as the single critical point at which the R_1 and R_2 facets coexist across static edges; see Eq. (2.10). However, as revealed in Sec. II, VA affects differently the concave uphill edges and concave downhill edges, so they become static at two distinct values of the system control parameter a_{convex} and a_{concave} which merge into a_{cr} in the zero VA limit; see our Eq. (2.37) and the discussion. For a nonzero VA, however, $a_{\mathrm{convex}} \neq a_{\mathrm{concave}}$. This seminal VA effect gives rise to the complex kinetic phase diagram in Fig. 7(b) involving the altered $R_1^{(\mathrm{rec})}$ state, the altered $R_2^{(\mathrm{rec})}$ state, and the extended ripple rotation transition range.

Focus of this study was on the ripple rotation transition involving the multistable region, seen in the epitaxial growth and erosion experiments on Ag(110) [1,2], in which R_1 facets $(\pm M_1,0)$ and R_2 facets $(0,\pm M_2)$ are both stable. An alternative scenario for this transition, anticipated in Ref. [4], and then observed on Rh(110) and Cu(110) surfaces [3], involves the intermediary rhomboidal pyramid (RhP) state. The RhP structures are 2D arrays of four sided pyramids and pyrami-

dal pits that have rhomboidal contour lines. The RhP state pyramids are comprised of facets which slope vectors form a quartet of four equivalent (symmetry related) slope vectors $(\pm M_1, \pm M_2)$ [4]. In accord with the experiments [3], the RhP state exhibits an enhanced roughening, with $\langle h^2 \rangle^{1/2} \sim t^{0.4}$, already with zero VA [4]. In addition, the SD and FT data for the RhP state obtained for zero VA [4], are qualitatively the same as the data obtained in the experiments on Rh(110) and Cu(110), [3]. Thus, the VA does not substantially alter the RhP state. Beyond this is the fact that the RhP four sided pyramids are made out of the quartet of four equivalent facets. By symmetry, such facets can coexist across static edges for whatever values of the system control parameter or of the VA. The VA produces only (purely quantitative) difference between the widths of the uphill and downhill edges on the four-sided pyramids and pits [see Ref. [6], for a similar VA effect on the (100) surfaces]. In contrast to the RhP pyramids, the rectangular rippled states have pyramids comprised of two types of facets R_1 at $(\pm M_1, 0)$ and R_2 at $(0, \pm M_2)$, which are oriented along the two nonequivalent principal axis of (110) (see SDs in our figures here). Such nonequivalent facets can coexist across static edges only at special values of the system control parameter which are affected by the VA. As discussed in this study, this fact prominently affects the structure, dynamics, and kinetic phase transitions of the interface for the systems in which the ripple rotation transition goes through the multistable system parameter region in which R_1 and R_2 facets are both stable.

One of our major points is that in the symmetry class of (110) surfaces, the VA can produce interface morphologies which are not present with zero VA. In this paper, we have supported this finding both by analytic arguments and by numerical simulations. On the other hand, VA effects on the symmetry class of (100) surfaces have not been explored with such a level rigor notwithstanding our brief discussions of VA effects on (100) surfaces in Ref. [6]. In that work, some striking VA morphological effects were observed in the numerical simulations within the so-called multi-P domain of the kinetic phase diagram of (100) surfaces. In those simulations, VA was seen to produce long lived yet only transient interfacial morphologies (with ultimate morphologies still being the same as for zero VA). Under some circumstances, however, these VA dominated morphologies persisted over time scales longer than simulation times of Ref. [6]. This suggests that VA on (100) surfaces also may produce ultimate (long times) interface morphologies which are not present for zero VA. However, no such a claim on (100) surfaces could had been made with full rigor in Ref. [6], due to lack of analytic arguments additionally supporting this suggestion from the simulations. Our present theoretical study on (110) surfaces, for which we could address VA more deeply, not only by simulations but also analytically, will certainly motivate a reconsideration of the VA role on (100) and (111) surfaces as well. They have higher symmetries than (110) and may be thus more susceptible to VA effects, possibly even more complex than those described in the present paper on (110) surfaces.

[1] F. Buatier de Mongeot, G. Costantini, C. Boragno, and U. Valbusa, Phys. Rev. Lett. **84**, 2445 (2000).

[2] G. Costantini, S. Rusponi, F. B. de Mongeot, C. Boragno, and U. Valbusa, J. Phys.: Condens. Matter **13**, 5875 (2001).

[3] A. Molle, F. B. de Mongeot, A. Molinari, F. Xiaerding, C. Boragno, and U. Valbusa, Phys. Rev. Lett. **93**, 256103 (2004); A. Molle, F. Buatier de Mongeot, A. Molinari, C. Boragno, and U. Valbusa, Phys. Rev. B **73**, 155418 (2006); see, also, F. Buatier de Mongeot, A. Toma, A. Molle, S. Lizzit, L. Petaccia, and A. Baraldi, Phys. Rev. Lett. **97**, 056103 (2006).

[4] L. Golubovic, A. Levandovsky, and D. Moldovan, Phys. Rev. Lett. **89**, 266104 (2002); A. Levandovsky, L. Golubovic, and D. Moldovan, Phys. Rev. E **74**, 061601 (2006).

[5] For reviews, see J. Krug, Adv. Phys. **46**, 139 (1997); Physica A **313**, 47 (2002); see also, J. W. Evans, P. A. Thiel, and M. C. Bartelt, Surf. Sci. Rep. **61**, 1 (2006); M. Li and J. W. Evans, Phys. Rev. Lett. **95**, 256101 (2005); **96**, 079902E (2006); Phys. Rev. B **73**, 125434 (2006).

[6] A. Levandovsky and L. Golubovic, Phys. Rev. B **69**, 241402(R) (2004).

[7] J. Villain, J. Phys. I **1**, 19 (1991).

[8] D. Moldovan and L. Golubovic, Phys. Rev. E **61**, 6190 (2000).

[9] M. Siegert, Phys. Rev. Lett. **81**, 5481 (1998).

[10] K. J. Caspersen, A. R. Layson, C. R. Stoldt, V. Fournee, P. A. Thiel, and J. W. Evans, Phys. Rev. B **65**, 193407 (2002). Side-by-side arranged four sided mounds were observed in these microscopic kinetic simulations of the Ag(100) surface. For the present less symmetric (110) surface, such side-by-side arranged pyramids, observed in our Fig. 5(d), are only approximately square shaped and packed as arrays between long straight pits, yielding the near in-phase diffraction pattern seen in Fig. 6(c) which is like that of a rippled state.

[11] For example, on (100) surfaces, positive VA values favor rounder tops of four-sided pyramids and sharper four-sided pyramidal pits (relative to zero VA morphologies with no difference between tops and pits widths). Experiments on (100) surfaces indeed reveal these features (i. e., a positive VA) to be typically realized. See the micrographs of the checkerboard structure of alternating four-sided pyramids and pyramidal pits on Cu(100) surface, in J.-K. Zuo and J. F. Wendelken, Phys. Rev. Lett. **78**, 2791 (1997). We stress that a similar effect of a positive VA is seen in its effects on the facet edges widths: convex edges are narrower whereas concave edges are broader relative to their widths at zero VA. See, for example, Eqs. (2.33) and (2.34), which imply $w_+ < w_-$ for $\lambda' > 0$.

[12] See, for example, in P. M. Chaikin and T. C. Lubensky, *Principles of Condensed Matter Physics* (Cambridge University Press, Cambridge, 1995), Chap. 10.